Prediction of the Elastic–Plastic Stress/Strain Response for Injection-Molded Long-Fiber Thermoplastics[1]

BA NGHIEP NGUYEN* AND SATISH K. BAPANAPALLI
Pacific Northwest National Laboratory, P.O. Box 999, Richland, WA 99352, USA

VLASTIMIL KUNC
Oak Ridge National Laboratory, P.O. Box 2009, Oak Ridge, TN 37831, USA

JAY H. PHELPS AND CHARLES L. TUCKER III
University of Illinois at Urbana-Champaign, Department of Mechanical Science and Engineering, Urbana, IL 61801, USA

ABSTRACT: This article proposes a model to predict the elastic–plastic response of injection-molded long-fiber thermoplastics (LFTs). The model accounts for elastic fibers embedded in a thermoplastic resin that exhibits the elastic–plastic behavior obeying the Ramberg–Osgood relation and *J*-2 deformation theory of plasticity. It also accounts for fiber length and orientation distributions in the composite formed by the injection-molding process. Fiber orientation was predicted using an anisotropic rotary diffusion model recently developed for LFTs. An incremental procedure using Eshelby's equivalent inclusion method and the Mori–Tanaka assumption is applied to compute the overall stress increment resulting from an overall strain increment for an aligned-fiber composite that contains the same fiber volume fraction and length distribution as the actual composite. The incremental response of the latter is then obtained from the solution for the aligned-fiber composite by averaging over all fiber orientations. Failure during incremental loading is predicted using the Van Hattum–Bernado model that is adapted to the composite elastic–plastic behavior. The model is validated against the experimental stress–strain results obtained for long-glass-fiber/polypropylene specimens.

KEY WORDS: long-fiber thermoplastics, injection molding, fiber length distribution, fiber orientation, elastic–plastic behavior, failure, strength.

*Author to whom correspondence should be addressed. E-mail: ba.nguyen@pnl.gov
Figure 1 appears in color online: http://jcm.sagepub.com
[1]This manuscript has been authored by Battelle Memorial Institute, Pacific Northwest Division, under Contract No. DE-AC06-76RL0 1830 with the U.S. Department of Energy. The United States Government retains and the publisher, by accepting the article for publication, acknowledges that the United States Government retains a non-exclusive, paid-up, irrevocable, world-wide license to publish or reproduce the published form of this manuscript, or allow others to do so, for United States Government purposes.

0021-9983/09/03 0217–30 $10.00/0 DOI: 10.1177/0021998308099219
© SAGE Publications 2009
Los Angeles, London, New Delhi and Singapore

Downloaded from jcm.sagepub.com at OAK RIDGE NATIONAL LABORATORY on October 5, 2015

INTRODUCTION

REDUCING VEHICLE WEIGHT to reduce energy consumption and engine emissions is one of the major objectives of the automotive industry. To this end, intensive research has been devoted to enable the use of lightweight materials for important structural applications. Long-fiber reinforced thermoplastics (LFTs) are among the prime candidate materials to be used as a substitute for steels. These composites, which can be produced by injection molding, present the advantage of relatively low-cost production and offer good mechanical performance in terms of stiffness, strength, creep and fatigue endurance. They are therefore suitable for structural applications. In a recent article, Nguyen et al. [1] pointed out that to use LFTs efficiently and safely for structural applications, it is essential to be able to (i) predict their microstructure as a function of the constituents' properties and characteristics as well as processing parameters, (ii) predict their thermoelastic properties and nonlinear responses as a function of the as-formed microstructure, and (iii) establish reliable characterization methods for obtaining all the necessary microstructural features for the model validation. Reference [1] described the effect of fiber length and orientation distributions on the elastic properties of LFTs. It also showed the limitation of existing fiber orientation models [2], and emphasized the need to develop a better model to predict fiber orientation in LFTs.

The present article extends the methodology developed in Ref. [1] to the computation of the nonlinear stress–strain response of LFTs up to the point of failure. There are two main causes of material nonlinear response in LFTs: plastic deformation of the thermoplastic matrix, and progressive damage due to matrix cracking, fiber/matrix debonding, fiber pull-out and rupture. This article addresses the material nonlinearities due to plastic deformation of the thermoplastic matrix. Progressive damage coupled with plasticity will be addressed in our future work on LFTs.

Previously, the elastic-damage behavior of discontinuous fiber polymer composites was modeled by Nguyen and Khaleel [3,4], and Nguyen et al. [5] using a mechanistic approach that combines micromechanics with continuum damage mechanics. In Refs [3–5], a reference composite was defined containing aligned fibers, and matrix microcracks that were modeled as ellipsoidal inclusions with zero stiffness. Fiber/matrix debonding was also accounted for in Ref. [5]. Next, the virgin and reduced elastic properties of the reference composite were computed using micromechanical models [6–9] and were then distributed over all possible orientations to obtain the properties of the random fiber composite containing random matrix microcracks. Finally, the macroscopic response of the random fiber composite subject to matrix cracking [3,4], or both matrix cracking and fiber/matrix debonding [5] was determined by means of a continuum damage mechanics formulation.

Thermoplastic resins such as polypropylene (PP) or polyethylene (PE) are semi-crystalline polymers whose microstructures possess an amorphous phase interleaved with crystalline lamellae, with macromolecular chains engaged in both phases. Plastic deformation in semi-crystalline polymers is a complex phenomenon occurring in both crystalline and amorphous phases [10]. For a polymer composite subjected to increasing load, the stress that is transferred to the matrix material induces plastic flow in the matrix, and as a consequence, causes irreversible inelastic strain for the composite.

The elastic–plastic behavior of short-fiber metal matrix composites was previously investigated using Eshelby's equivalent inclusion method [6] and the Mori–Tanaka mean-field approach [7] (see also Refs [11–15]). In this article, the combination of Eshelby's equivalent

Downloaded from jcm.sagepub.com at OAK RIDGE NATIONAL LABORATORY on October 5, 2015

inclusion method with the Mori–Tanaka model is termed the *Eshelby–Mori–Tanaka approach* (EMTA). Arsenault and Taya [11] used the EMTA to calculate residual stresses in metal matrix composites containing aligned elastic short-fibers in an elastic–plastic matrix that was described by a bilinear model. About the same time, Tandon and Weng [12] developed an EMTA-based theory to predict the elastic–plastic behavior of particle reinforced materials. The particles considered in Ref. [12] were elastic while the matrix was elastic–plastic and obeyed the modified Ludwik equation. Also, explicit expression of the matrix secant modulus was defined and used in the EMTA homogenization to compute the composite response. Dunn and Ledbetter [13] used a similar model and the expression of the matrix effective stress established by Qui and Weng [14] (which was based on an energy approach) to compute the elastic–plastic stress/strain response of textured short-fiber composites. In Ref. [14], fiber orientation was described by orientation distribution functions of Euler's angles. Later, Pettermann et al. [15] developed an incremental EMTA procedure to predict the thermo-elastic-plastic behavior of composites containing aligned thermo-elastic spheroidal inclusions in a thermo-elastic-plastic matrix whose behavior was described by the *J*-2 flow theory with isotropic hardening. These authors calculated the instantaneous Eshelby tensor numerically by a method developed by Gavazzi and Lagoudas [16] to account for the anisotropic structure of the matrix material in the plastic regime. Doghri and Ouaar [17] developed homogenization schemes and numerical algorithms for two-phase elastic–plastic composites. In particular, these authors investigated the issue of tangent operators used in constitutive laws. Their composite stress–strain results which were obtained using the *isotropic part* of the matrix tangent stiffness tensor to compute the instantaneous Eshelby's tensor agreed well with their predictions based on a unit cell finite element analysis. Doghri and Tinel [18,19] proposed a two-step incremental formulation for a mean-field homogenization approach to predict the stress–strain response of multiphase elastic–plastic materials reinforced with non-spherical and non-aligned inclusions whose orientation was described using an orientation distribution function. In the first step, the composite reference volume element is decomposed into a set of pseudo-grains, homogenization is then carried out for each pseudo grain using a Hill-type incremental formulation. The second step conducts homogenization over all pseudo-grains. More recently, Pierard et al. [20] confirmed Doghri and Ouaar's findings [17] regarding the use of an isotropic Eshelby's tensor when assessing the accuracy of the prediction of the composite elastic–plastic response using the secant or incremental approaches. They have found that the second-order secant approach and the incremental approach that used the Eshelby's tensor computed based on the isotropic part of the matrix tangent stiffness tensor provided the best approximations of their numerical stress–strain results. These were obtained by numerical simulations of a composite representative volume element containing ellipsoidal inclusions.

In view of all the previous studies, this article applies an incremental EMTA procedure to predict the elastic–plastic stress–strain response of long-fiber thermoplastics. It is assumed that the fibers are linear elastic while the elastic–plastic matrix is isotropic and obeys the Ramberg–Osgood relation [21] and the *J*-2 deformation theory of plasticity. An incremental EMTA procedure is then developed to compute the (homogenized) overall stress increment resulting from an overall strain increment for a unidirectional (UD) fiber composite, which is termed the *reference composite*. The key idea is to replace the elastic modulus of the matrix material in the elastic problem by its instantaneous tangent modulus, as determined from the Ramberg–Osgood relation and *J*-2 deformation theory. Next, the elastic–plastic response of the actual LFT composite is obtained by averaging the behavior of the reference composite over all fiber orientations using the orientation averaging method [22,23].

Downloaded from jcm.sagepub.com at OAK RIDGE NATIONAL LABORATORY on October 5, 2015

This method offers an efficient way to account for fiber orientation distribution in the composite. Failure during loading is predicted using the Van Hattum–Bernado model [24], which is adapted to the elastic–plastic behavior of the composite. Van Hattum and Bernado expressed the Tsai–Wu's failure criterion [25] in terms of fiber and matrix strengths as well as fiber orientation tensor components. The extension of this model to the composite elastic–plastic behavior requires defining an '*equivalent linear elastic*' composite at each load increment.

Although incremental EMTAs have been previously used for various composite systems, their application to model the elastic–plastic behavior of LFTs has not been conducted. This is one of the focuses of this article. Also, this article adapts the Van Hattum–Bernado model to an incremental EMTA to predict strength of LFTs. In addition, a particular focus is on fiber orientation and length distributions, which greatly influence the composite's properties and response. We will show the useful application of a new fiber orientation model (termed the *anisotropic rotary diffusion* (ARD) model) recently developed by Phelps and Tucker for LFTs [26].

Long-glass-fiber/PP specimens were cut from injection-molded samples for mechanical characterization and testing. Fiber length and orientation distributions were measured at several selected locations for use in the computation. A two-parameter Weibull distribution [1] or a log-normal distribution can be used to represent the probability density function for weight of fiber vs. fiber length. Although Weibull's distribution is sufficiently accurate for computation of elastic properties, the log-normal distribution is more appropriate for strength prediction. Fiber orientation distributions in the samples were predicted using the ARD model. The elastic–plastic and strength prediction model was implemented in the ABAQUS finite element code by means of user subroutines. ABAQUS was then used to compute the elastic–plastic response and strength of LFT glass/PP specimens. The computed responses using the predicted fiber orientation results are compared with the solutions obtained based on measured fiber orientations, and with the experimental stress–strain results.

THEORY

This section develops an elastic–plastic model for LFTs, making use of an incremental EMTA procedure to compute the composite stress–strain response. The model accounts for fiber length and orientation distribution resulting from the injection-molding process. The reader is referred to Ref. [1] for a detailed description of fiber length distribution (FLD) and Refs [1] and [22] for the definition of the orientation tensors. This section also provides a summary of the Van Hattum–Bernado model [24] that is used in conjunction with the elastic–plastic model to predict strength of LFTs. A summary of the Phelps–Tucker's anisotropic rotary diffusion model [26] to predict fiber orientation in LFTs is also presented.

An Elastic–Plastic Model for LFTs

Consider a unidirectional (UD) fiber composite containing a fiber length distribution. Computation of the incremental elastic–plastic response of the composite starts from the EMTA solution for the elastic composite, which is given by:

$$\mathbf{H} = \frac{\int_0^\infty \mathbf{H}^*(l/d)p(l)\mathrm{d}l}{\int_0^\infty p(l)\mathrm{d}l} \tag{1}$$

Downloaded from jcm.sagepub.com at OAK RIDGE NATIONAL LABORATORY on October 5, 2015

with:

$$\mathbf{H}^* = \mathbf{H}_\mathrm{m} + v_\mathrm{f}(\mathbf{H}_\mathrm{f} - \mathbf{H}_\mathrm{m}) : \mathbf{A}_\mathrm{f} \tag{2}$$

where $\mathbf{H}^*(l/d)$ is the stiffness matrix of the UD composite having the fiber aspect ratio l/d, where l is the fiber length and d is the fiber diameter. $P(l)$ is the probability density function (PDF) that expresses the fiber length distribution (FLD) in terms of number or weight of fibers vs. fiber length. v_f is the fiber volume fraction. $\mathbf{H}$, $\mathbf{H}_\mathrm{m}$, and $\mathbf{H}_\mathrm{f}$ are the stiffness tensors of the UD composite, matrix, and fiber phases, respectively. $\mathbf{A}_\mathrm{f}$ is the fiber strain-concentration tensor, given by:

$$\mathbf{A}_\mathrm{f} = \mathbf{T} : [(1 - v_\mathrm{f})\mathbf{I} + v_\mathrm{f}\mathbf{T}]^{-1} \tag{3}$$

with:

$$\mathbf{T} = \left[\mathbf{I} + \mathbf{S} : \mathbf{H}_\mathrm{m}^{-1} : (\mathbf{H}_\mathrm{f} - \mathbf{H}_\mathrm{m})\right]^{-1} \tag{4}$$

where $\mathbf{S}$ is the Eshelby tensor and $\mathbf{I}$ is the fourth-order identity tensor. Next, the orientation averaging method is applied to Equation (1) to obtain the stiffness tensor $\overline{\mathbf{H}}$ for the actual composite possessing a fiber orientation distribution (FOD). The result is written (using index notation) as [22,23]:

$$\begin{aligned}\overline{H}_{ijkl} = {} & B_1\tilde{A}_{ijkl} + B_2(A_{ij}\delta_{kl} + A_{kl}\delta_{ij}) + B_3(A_{ik}\delta_{jl} + A_{il}\delta_{jk} + A_{jk}\delta_{il}) \\ & + B_4\delta_{ij}\delta_{kl} + B_5(\delta_{ij}\delta_{jl} + \delta_{il}\delta_{jk})\end{aligned} \tag{5}$$

where the coefficients B_i $(i = 1, \ldots, 5)$ are the invariants of the UD stiffness tensor. A_{ij} and $\tilde{A}_{ijkl}$ are the second and fourth-order orientation tensors, respectively, and δ_{ij} is the identity tensor. A_{ij} is either predicted by a process model or measured, and then the ORE orthotropic closure approximation [27,28] is used to estimate the fourth-order tensor $\tilde{A}_{ijkl}$ from A_{ij}.

When the material behavior is nonlinear, we look for an incremental solution of the form:

$$\Delta\sigma = \overline{\mathbf{H}}^\mathrm{t} : \Delta\boldsymbol{\varepsilon} \tag{6}$$

in which $\Delta\boldsymbol{\sigma}$ is the composite stress increment resulting from the composite strain increment $\Delta\boldsymbol{\varepsilon}$, and $\overline{\mathbf{H}}^\mathrm{t}$ is the current tangent stiffness tensor of the composite. To compute the stress–strain response of the composite incrementally, it is necessary to calculate $\overline{\mathbf{H}}^\mathrm{t}$ at each increment. To do so, the key idea is to replace the elastic stiffness tensor $\mathbf{H}_\mathrm{m}$ of the matrix in Equations (2) and (4) by its current tangent stiffness tensor $\overline{\mathbf{H}}_\mathrm{m}^\mathrm{t}$ (which reflects the nonlinear behavior of the matrix) and apply the EMTA homogenization procedure to obtain $\overline{\mathbf{H}}^\mathrm{t}$. The computational method is as follows. The Ramberg–Osgood relation is used to describe the elastic–plastic behavior of the matrix in terms of the total matrix equivalent stress ($\overline{\sigma}_\mathrm{m}$) and strain ($\overline{\varepsilon}_\mathrm{m}$):

$$\overline{\varepsilon}_\mathrm{m} = \overline{\varepsilon}_\mathrm{m}^\mathrm{e} + \overline{\varepsilon}_\mathrm{m}^\mathrm{p} = \frac{\overline{\sigma}_\mathrm{m}}{E_\mathrm{m}} + \left(\frac{\sigma_0}{E_\mathrm{m}}\right)\left(\frac{\sigma_\mathrm{m}}{\sigma_0}\right)^n \tag{7}$$

Downloaded from jcm.sagepub.com at OAK RIDGE NATIONAL LABORATORY on October 5, 2015

where σ_0 and n are material coefficients and are known as the reference stress and the power-law exponent E_m, $\bar{\varepsilon}_m^e$, and $\bar{\varepsilon}_m^p$ are the matrix elastic modulus, equivalent elastic strain, and equivalent plastic strain, respectively. The overall strain increment applied to the composite induces the strain increments in the fiber and matrix phases as follows:

$$\Delta\boldsymbol{\varepsilon}_f = \overline{\mathbf{A}}_f : \Delta\boldsymbol{\varepsilon} \tag{8}$$

$$\Delta\boldsymbol{\varepsilon}_m = \mathbf{A}_m : \Delta\boldsymbol{\varepsilon}. \tag{9}$$

Here $\overline{\mathbf{A}}_f$ is the orientation average of $\mathbf{A}_f$ that is obtained by applying the orientation averaging method to Equation (3). The matrix strain concentration tensor $\mathbf{A}_m$ is related to $\overline{\mathbf{A}}_f$ as:

$$(1 - v_f)\mathbf{A}_m + v_f\overline{\mathbf{A}}_f = \mathrm{I}. \tag{10}$$

The matrix equivalent plastic strain at the end of the previous increment is saved and used at the beginning of the current increment to compute the *plastic modulus* E_m^p of the matrix based on the Ramberg–Osgood representation:

$$E_m^p = \frac{d\bar{\sigma}_m}{d\bar{\varepsilon}_m^p} = \frac{E_m^{1/n}\sigma_0^{(n-1)/n}(\bar{\varepsilon}_m^p)^{(1-n)/n}}{n}. \tag{11}$$

Hence, the current tangent modulus of the matrix is determined as:

$$E_m^t = \frac{E_m E_m^p}{E_m + E_m^p} = \frac{E_m}{1 + n\sigma_0^{1-n}\bar{\sigma}_m^{n-1}}. \tag{12}$$

The computation of the current matrix tangent modulus allows calculation of the current matrix tangent stiffness tensor $\mathbf{H}_m^t$, and therefore, the current tangent stiffness tensor of the composite ($\overline{\mathbf{H}}^t$) can be determined using Equations (1), (2), and (5). Next, the matrix stress increment is calculated as:

$$\Delta\boldsymbol{\sigma}_m = \mathbf{H}_m^t : \Delta\boldsymbol{\varepsilon}_m. \tag{13}$$

The matrix stress is then updated, and the matrix equivalent stress is obtained using the J-2 deformation theory of plasticity:

$$\bar{\sigma}_m = \sqrt{\frac{3}{2}\sigma_{ij}^{\prime m}\sigma_{ij}^{\prime m}}. \tag{14}$$

where σ_{ij}^m is the matrix deviatoric stress tensor. The computation of $\bar{\sigma}_m$ allows the current matrix equivalent strain and plastic strain to be determined using the Ramberg–Osgood relation (7). These quantities are saved to start the next increment of the loading process. Finally, the overall stress increment is computed by Equation (6) to update the overall stress at the end of the current increment. At each load increment, failure is predicted using the Van Hattum–Bernado model [24], which is summarized in the next section.

The elastic–plastic EMTA procedure was implemented into the ABAQUS finite element code by means of user subroutines. The UMAT subroutine was employed to implement

Downloaded from jcm.sagepub.com at OAK RIDGE NATIONAL LABORATORY on October 5, 2015

the constitutive model. In addition, the utility user subroutine UEXTERNALDB was used to read the fiber orientation and FLD data obtained from experiments or process modeling. In UMAT, three options for fiber length distribution are introduced: the use of the experimental FLD, the use of Weibull or log-normal distributions whose shape parameters are introduced as material constants. The 'User Material' option of ABAQUS is used to introduce the material input data for the model.

Prediction of the Composite Strength

Van Hattum and Bernado [24] first applied the Tsai–Wu criterion [25] to a UD fiber composite that contains a fiber length distribution. This criterion predicts failure when:

$$f = \mathbf{F} : \boldsymbol{\sigma} + \boldsymbol{\sigma}^T : \tilde{\mathbf{F}} : \boldsymbol{\sigma} = 1 \tag{15}$$

where $\mathbf{F}$ and $\tilde{\mathbf{F}}$ are the second and fourth-order strength tensors, respectively, and $\boldsymbol{\sigma}$ is the stress tensor. If the behavior of the UD composite is the same in tension and compression (i.e., its tensile and compressive strengths are the same), then $\mathbf{F} = 0$. The components of $\tilde{\mathbf{F}}$ can then be determined in terms of the strengths of the UD composite, which are obtained here using the Kelly–Tyson model [29]. The details of the derivation to obtain the components of $\tilde{\mathbf{F}}$ are provided in Ref. [24].

$$\tilde{\mathbf{F}} = \tilde{\mathbf{F}}(\sigma_{\mathrm{L}}, \sigma_{\mathrm{T}}, \tau_{\mathrm{s}}) \tag{16}$$

where σ_{L}, σ_{T}, and τ_{s} are the longitudinal, transverse, and shear strengths of the UD fiber composite, respectively.

The longitudinal strength is predicted using

$$\sigma_{\mathrm{L}} = \int_0^{l_{\mathrm{c}}} \sigma_{\mathrm{L}}^*(l) p(l) \mathrm{d}l + \int_{l_{\mathrm{c}}}^{\infty} \sigma_{\mathrm{L}}^*(l) p(l) \mathrm{d}l \tag{17}$$

in which l_{c} is the *critical fiber length* necessary to build up sufficient stress to break a fiber. $p(l)$ is the PDF for fiber length, as in Equation (1) σ_{L}^* is given by the Kelly–Tyson model in terms of the interfacial shear strength τ, the equivalent stress developed in the matrix at fiber failure strain σ_{m}^*, and fiber strength σ_{f}:

$$\begin{aligned} \sigma_{\mathrm{L}}^* &= v_{\mathrm{f}} \frac{\tau l}{d} + \sigma_{\mathrm{m}}^*(1 - v_{\mathrm{f}}) \quad \text{for } l < l_{\mathrm{c}} \\ \sigma_{\mathrm{L}}^* &= v_{\mathrm{f}} \sigma_{\mathrm{f}} \left(1 - \frac{l_{\mathrm{c}}}{2l}\right) + \sigma_{\mathrm{m}}^*(1 - v_{\mathrm{f}}) \quad \text{for } l \geq l_{\mathrm{c}}. \end{aligned} \tag{18}$$

For a strong interfacial bond, the transverse strength of the UD composite is approximated by the strength of the matrix, $\overline{\sigma}_{\mathrm{m}}^s$, and its shear strength is then determined by: $\tau_m = \overline{\sigma}_{\mathrm{m}}^s / \sqrt{3}$. Due to processing, the actual composite can suffer from poorer fiber/matrix interface properties, and as a result, the interfacial shear strength can be significantly lower than the shear strength of the matrix material.

Downloaded from jcm.sagepub.com at OAK RIDGE NATIONAL LABORATORY on October 5, 2015

For a UD linear elastic composite, Equation (15) can also be expressed in terms of strains as:

$$f = \mathbf{G} : \boldsymbol{\varepsilon} - \boldsymbol{\varepsilon}^T : \tilde{\mathbf{G}} : \boldsymbol{\varepsilon} = 1 \tag{19}$$

where:

$$\mathbf{G} = \mathbf{F} : \mathbf{H}_{\mathrm{eq}} \tag{20}$$

and:

$$\tilde{\mathbf{G}} = \mathbf{H}_{\mathrm{eq}}^T : \tilde{\mathbf{F}} : \mathbf{H}_{\mathrm{eq}} \tag{21}$$

with $\mathbf{H}_{\mathrm{eq}} = \mathbf{H}$, the stiffness tensor of the UD composite given by Equation (1). To extend the criterion (15) to a random-fiber composite that possesses a fiber orientation distribution, we assume that the composite consists of an aggregate of UD elements with different orientations, and that local failure occurs when the average value of f among all elements equals unity. Consistent with our averaging scheme for stress, we assume that each element of the aggregate experiences the same strain. Thus, we apply the orientation averaging method [22,23] to Equation (21) [24] to find

$$\overline{\tilde{\mathbf{F}}} = \overline{\mathbf{H}}_{\mathrm{eq}}^{-T} : \overline{\tilde{\mathbf{G}}} : \overline{\mathbf{H}}_{\mathrm{eq}}^{-1} \tag{22}$$

where the 'bar' symbol denotes orientation averaging, and $\overline{\mathbf{H}}$ is given by Equation (5) for an elastic composite. The failure criterion (15) then becomes:

$$f = \boldsymbol{\sigma}^T : \overline{\tilde{\mathbf{F}}} : \boldsymbol{\sigma} = 1. \tag{23}$$

For a composite that exhibits an elastic–plastic response, some approximation is required. Here, we determine $\mathbf{H}_{\mathrm{eq}}$ as follows. At the end of each load increment, we define an 'equivalent UD composite' and compute its stiffness. First, the computed equivalent strain and equivalent stress of the matrix material at the end of the current increment are used to define the current *matrix secant modulus*, $E_{\mathrm{m}}^{s} = \overline{\sigma}_{\mathrm{m}}/\overline{\varepsilon}_{\mathrm{m}}$. Next, the EMTA procedure is applied to obtain the stiffness of the equivalent UD composite that has elastic fibers and an elastic matrix of modulus E_{m}^{s}. This stiffness tensor is then used in Equations (20) and (21). As the failure criterion ignores the loading history, using the as-defined equivalent composite is a way to bring the UD elastic–plastic composite to the same current stress state at which the correspondence between the strength tensors given by Equations (20) and (21) still holds as in the elastic case. However, we implicitly account for the nonlinear behavior of the composite in the criterion via the stress state. Finally, the application of the orientation averaging method allows the strength tensors of the actual elastic–plastic composite to be determined.

In our elastic–plastic EMTA procedure, the overall stress at the end of each increment is used to evaluate criterion (23). If the failure criterion is verified for a given integration

Downloaded from jcm.sagepub.com at OAK RIDGE NATIONAL LABORATORY on October 5, 2015

point, the composite stress and stiffness at this point are reduced to zero in a small number of load steps using a vanishing element technique [5]:

$$
\begin{aligned}
n < K &: \overline{\mathbf{H}}^{\mathrm{t}}_{\mathrm{failure}} = \overline{\mathbf{H}}^{\mathrm{t}}(f=1) - \frac{n\overline{\mathbf{H}}^{\mathrm{t}}(f=1)}{K} \\
n \geq K &: \overline{\mathbf{H}}^{\mathrm{t}}_{\mathrm{failure}} = \boldsymbol{\alpha}
\end{aligned}
\tag{24}
$$

where $\overline{\mathbf{H}}^{\mathrm{t}}(f=1)$ is the composite stiffness at the point of failure ($f=1$), n is the load step number starting from the step at which failure occurs, and K is a prescribed value. The components of $\boldsymbol{\alpha}$ are taken to be very small ($\sim 10^{-8}$ MPa) to represent a vanishing stiffness. It is necessary that the stiffness and stress reduction to zero occurs progressively in a number of steps to avoid numerical convergence problems.

Prediction of Fiber Orientation

Predicting flow-induced fiber orientation in short-fiber systems has been carried out for more than two decades using the Folgar–Tucker model [30]. In this model, the effects of fiber–fiber interactions, which occur in nondilute fiber suspensions and whose effect is to reduce the fiber aligment, are captured by an isotropic rotary diffusion term governed by a scalar interaction coefficient C_{I}. More recently, some efforts have been made to improve the Folgar–Tucker model for concentrated short-fiber systems. This has led to the so-called *reduced strain closure* (RSC) model [2], which contains an additional empirical coefficient κ to reduce the *rate* of fiber aligment in a concentrated fiber suspension. An assessment of the RSC model [1] showed that using a large value of the interaction coefficient C_{I} in the RSC model could give a correct prediction of the flow-direction orientation A_{11}. However, the thickness-direction component, A_{33}, was then over-predicted, resulting in the under-prediction of the cross-flow component A_{22}. Therefore, it was necessary to develop a better fiber orientation model for LFTs.

Fan et al. [31] and Phan-Thien et al. [32] proposed a fiber orientation model using an anisotropic rotary diffusion (ARD) term. However, the Phan-Thien/Fan model's diffusion term fails to return the fibers to an isotropic orientation at steady state, a necessary condition of any diffusion model. To correct the Phan-Thien/Fan model, Phelps and Tucker developed an expression for rotary diffusion that was defined on the surface of the unit sphere traced by all orientations of the unit orientation vector [26]. The expression for the ARD model to properly match the LFT fiber orientation data is:

$$
\begin{aligned}
\dot{\mathbf{A}} = {} & (\mathbf{W}\cdot\mathbf{A} - \mathbf{A}\cdot\mathbf{W}) + \xi(\mathbf{D}\cdot\mathbf{A} + \mathbf{A}\cdot\mathbf{D} - 2\tilde{\mathbf{A}}:\mathbf{D}) \\
& + \dot{\gamma}(2\mathbf{C} - 2(\mathrm{tr}\mathbf{C})\mathbf{A} - 5(\mathbf{C}\cdot\mathbf{A} + \mathbf{A}\cdot\mathbf{C}) + 10\tilde{\mathbf{A}}:\mathbf{C})
\end{aligned}
\tag{25}
$$

where $\mathbf{A}$ and $\tilde{\mathbf{A}}$ are the second- and fourth-order orientation tensors, respectively. $\dot{\mathbf{A}}=\mathbf{DA}/\mathrm{D}t$ with t being the time, $\mathbf{W}$ is the vorticity tensor, and $\mathbf{D}$ is the rate-of-deformation tensor.

Downloaded from jcm.sagepub.com at OAK RIDGE NATIONAL LABORATORY on October 5, 2015

$\dot{\gamma}$ is the scalar magnitude of $\mathbf{D}$, and ξ is the particle shape parameter ($\xi = 1$ for slender fibers). The rotary diffusion tensor $\mathbf{C}$ is constructed from the $\mathbf{A}$ and $\mathbf{D}$ tensors as:

$$\mathbf{C} = b_1\mathbf{I} + b_2\mathbf{A} + b_3\mathbf{A}^2 + b_4\frac{\mathbf{D}}{\dot{\gamma}} + b_5\frac{\mathbf{D}^2}{\dot{\gamma}^2} \tag{26}$$

where b_i ($i = 1, \ldots, 5$) are the scalar constants. A systematic method of selecting the b_is was developed in Ref. [26] to ensure stable and valid orientation solutions.

To properly match experimental orientation data, one may also need to slow the orientation kinetics of a given model. For instance, the RSC model [2] can objectively slow the orientation kinetics of the Folgar–Tucker model. Treating the ARD model similarly, the ARD–RSC model is then obtained as [26]:

$$\begin{aligned}\dot{\mathbf{A}}^{\mathrm{ARD-RSC}} &= (\mathbf{W}\cdot\mathbf{A} - \mathbf{A}\cdot\mathbf{W}) \\ &\quad + \xi(\mathbf{D}\cdot\mathbf{A} + \mathbf{A}\cdot\mathbf{D} - 2[\tilde{\mathbf{A}} + (1-\kappa)(\tilde{\mathbf{L}} - \tilde{\mathbf{M}} : \tilde{\mathbf{A}})] : \mathbf{D}) \\ &\quad + \dot{\gamma}\Big(2\Big[\mathbf{C} - (1-\kappa)\tilde{\mathbf{M}} : \mathbf{C}\Big] - 2\kappa\mathrm{tr}\mathbf{C}\Big)\mathbf{A} \\ &\quad - 5\Big(\mathbf{C}\cdot\mathbf{A} + \mathbf{A}\cdot\mathbf{C}) + 10\Big[\tilde{\mathbf{A}} + (1-\kappa)(\tilde{\mathbf{L}} - \tilde{\mathbf{M}} : \tilde{\mathbf{A}})\Big] : \mathbf{C}\Big)\end{aligned} \tag{27}$$

where $\mathbf{C}$ is given by Equation (26). $\tilde{\mathbf{L}}$ and $\tilde{\mathbf{M}}$ are fourth-order tensors that are defined by the eigenvalues and eigenvectors of $\mathbf{A}$. κ (<1) is a scalar parameter that controls the rate of fiber alignment.

EXPERIMENTAL METHODS AND MATERIALS

Molding Conditions and Material Characterization

This article uses the same material as our previous study [1]. Long-glass-fiber/polypropylene compounds were procured from Montsinger Technologies. The molding compound had a fiber weight fraction of 40%, a nominal fiber length of 13 mm, and a nominal fiber diameter of 17.4 μm. Injection molding was carried out for the center-gated disk and ISO-plaque geometries. The pellets were injected using two different volume flow rates (16.4 and 131.1 cm^3/s) in order to study the effect of the injection speed on the as-formed composite microstructure. In this article, these flow rates are denoted as slow-fill and fast-fill, respectively. The density of glass/polypropylene in the melt state is 1.2203 $\mathrm{g/cm}^3$. The weight fraction of glass fibers for both geometries is 40%, corresponding to 19.2% fiber volume fraction. The center-gated disk is 3 mm thick and has a diameter of 177.8 mm. The ISO-plaque is also 3mm thick, and is 90 mm long and 80 mm wide.

Figures 1 and 2 present the pictures of these injection-molded samples. Three regions were considered for fiber length and orientation measurements. These are denoted as A, B and C, and are located at 6, 34, and 64 mm from the gate on the center-gated disk, and at 15, 45, and 75 mm from the gate on the ISO plaque. A population of 2000 fibers was taken in each region for fiber length measurement. The FLD measurement method is described in Ref. [33] and summarized in Ref. [1]. Also, fiber orientation measurement was achieved using the optical system developed by Hine et al. [34]. The discussion on Hine et al.'s method (termed as the Leeds system) and its application to LFTs are provided in Ref. [1].

Downloaded from jcm.sagepub.com at OAK RIDGE NATIONAL LABORATORY on October 5, 2015

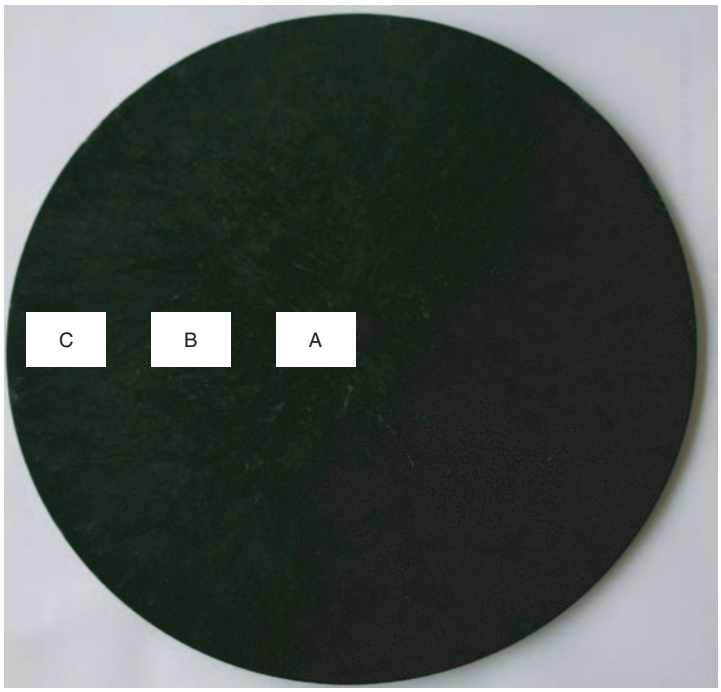

Figure 1. *The 3 mm thick injection-molded glass/PP center-gated disk: Regions A, B, and C being 25.4 mm long along a radial direction were taken for fiber length and orientation measurements.*

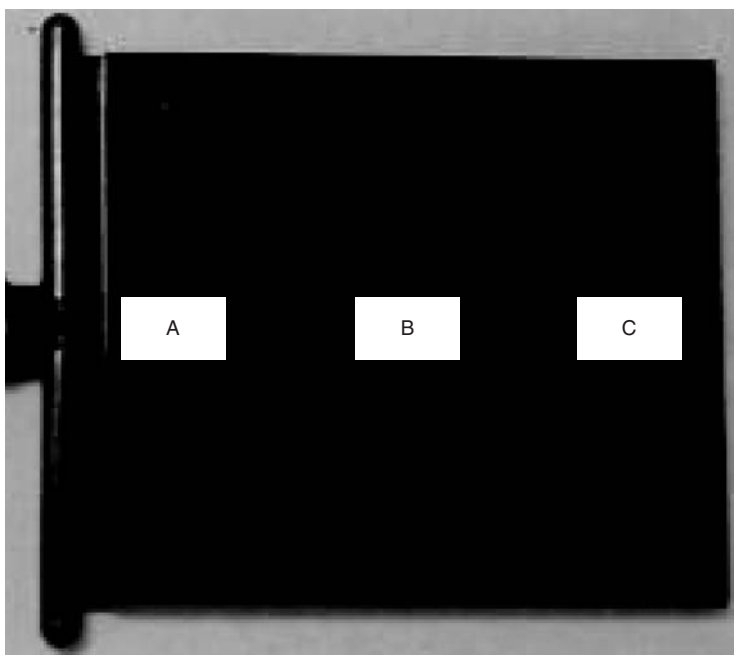

Figure 2. *The 3 mm thick injection-molded ISO-plaque: Regions A, B, and C being 25.4 mm long were taken for fiber length and orientation measurements.*

Downloaded from jcm.sagepub.com at OAK RIDGE NATIONAL LABORATORY on October 5, 2015

Stress–Strain Response Measurement

Tensile specimens were cut from the injection-molded samples for mechanical testing. For the ISO-plaque geometry, cuts were made out along the plaque's longitudinal (flow) and in-plane transverse (cross-flow) directions to remove specimens for the longitudinal and in-plane transverse stress–strain responses, respectively. The specimens that contain the sample edge were excluded from testing to avoid edge effects. For the center-gated disk geometry, the specimen was cut along the radial (flow) direction to obtain the specimens for determining the longitudinal response, while the in-plane transverse (cross-flow) response was obtained using a specimen that contains the location B in its central region, and whose long axis is perpendicular to the radial direction passing through this location. All specimens are 12.5 mm wide and 76 mm long. A servo-hydraulic machine applied tension at constant displacement rate of 0.0254 mm/s resulting in a constant strain rate of 3.342E−4/s. Strain was measured with a 12.5 mm gauge length extensometer positioned over the area of interest, while engineering stress was calculated from the load cell signal and the original cross-sectional area of the specimen.

RESULTS AND DISCUSSION

Fiber Length Distribution Results

Fiber length distributions for the studied samples were measured at the selected locations A, B, and C (see Figures 1 and 2) using the measurement method described in Ref. [33] and summarized in Ref. [1]. The raw FLD data was then corrected by the method presented in Ref. [33] to obtain an unbiased FLD. In Ref. [1] we showed that a two-parameter Weibull's distribution can globally well represent the corrected FLD in terms of a PDF for weight of fibers vs. fiber length, and that using the Weibull distribution to predict elastic moduli led to practically the same results as the use of the actual FLD. However, the effect of fiber length on strength of LFTs was not studied in Ref. [1], it is therefore necessary to assess Weibull's representation for FLDs in the prediction of the composite's stress–strain responses up to failure. Weibull's probability density function is given by:

$$p(l) = \frac{c}{b}\left(\frac{l}{b}\right)^{c-1} \mathrm{e}^{\left(\frac{l}{b}\right)^{c}} \tag{28}$$

where b and c are shape parameters that can be determined by a method based on the maximum likelihood technique, presented in Ref. [1]. A close examination of Weibull's fit for FLDs in Ref. [1] shows that Weibull's representation overestimates the weight contribution of the intermediate fiber length range (~2–3 mm) and underestimates the contribution of longer fibers (>4 mm). However, these longer fibers improve the overall strength of the composite, and therefore, it is necessary to use another representation of the FLD to better capture the long fiber range. To this end, the log-normal distribution can be used. The log-normal probability density function reads:

$$p(l) = \frac{1}{ls\sqrt{2\pi}} \exp\left(\frac{(\ln(t) - \mu)^2}{2s^2}\right) \tag{29}$$

Downloaded from jcm.sagepub.com at OAK RIDGE NATIONAL LABORATORY on October 5, 2015

where l is the fiber length, s is the shape parameter, and μ is the scale parameter. The two parameters are determined by using the experimental measurements combined with the maximum likelihood estimation technique to obtain the relations:

$$\mu = \frac{\sum_i \ln l_t}{N} \tag{30}$$

$$s^2 = \frac{\sum_i (\ln l_i - \mu)^2}{N}. \tag{31}$$

The lengths l_i span the range of the data, and N is total number of fibers for the whole range. Figures 3 and 4 present the FLDs for the fast-fill center-gated disk and ISO plaque, while Figures 5 and 6 show the FLDs for samples molded under slow-fill conditions. These figures also show the Weibull and log-normal fits, as well as the weight-average fiber lengths L_W, L_W^{Weib}, and $L_W^{\text{log-normal}}$ based on the corrected FLD, Weibull's fit, and log-normal fit, respectively. The Weibull distribution globally captures the FLD in terms of PDF for weight of fibers vs. fiber length, but better fits are obtained with the log-normal distribution. As expected, the slow injection rate reduces fiber length attrition and thus conserves longer fibers in the samples, however, when comparing Figures 3–5 and Figures 4–6, it is found that the injection rate effect is more important for the ISO-plaques.

Fiber Orientation Distribution Results

The ARD–RSC model summarized in the Theory section was implemented in ORIENT, a finite difference injection mold filling simulation [35], and ORIENT was

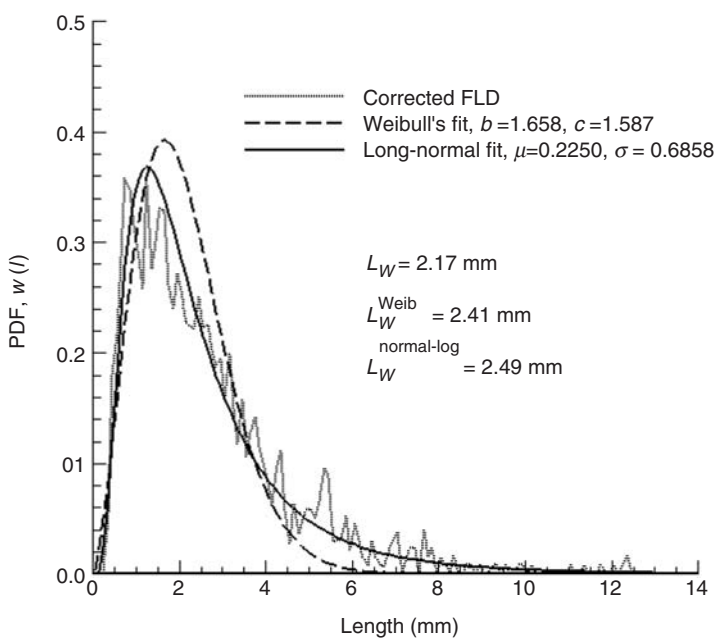

Figure 3. *FLDs in terms of probability density function for weight of fibers vs. fiber length for the fast-fill center-gated disk (Region B).*

Downloaded from jcm.sagepub.com at OAK RIDGE NATIONAL LABORATORY on October 5, 2015

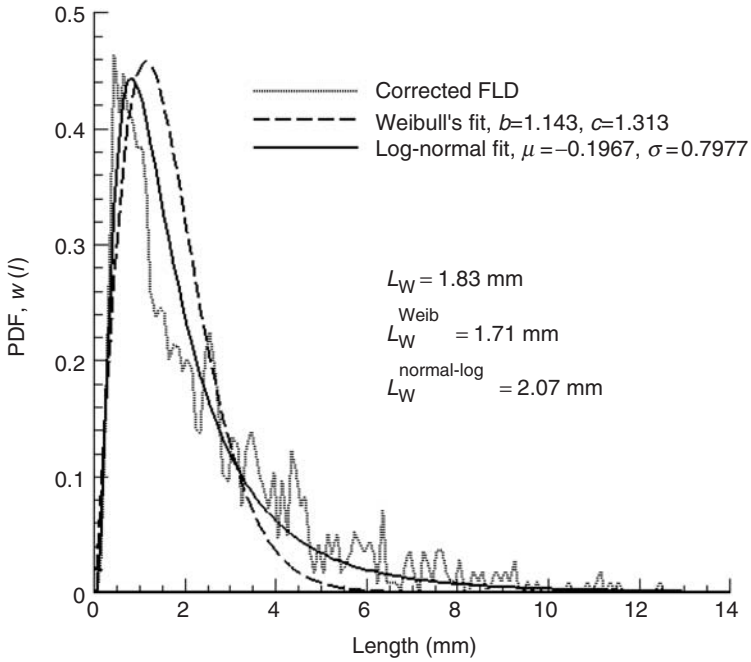

Figure 4. *FLD in terms of probability density function for weight of fibers vs. fiber length for the fast-fill ISO-plaque (Region B).*

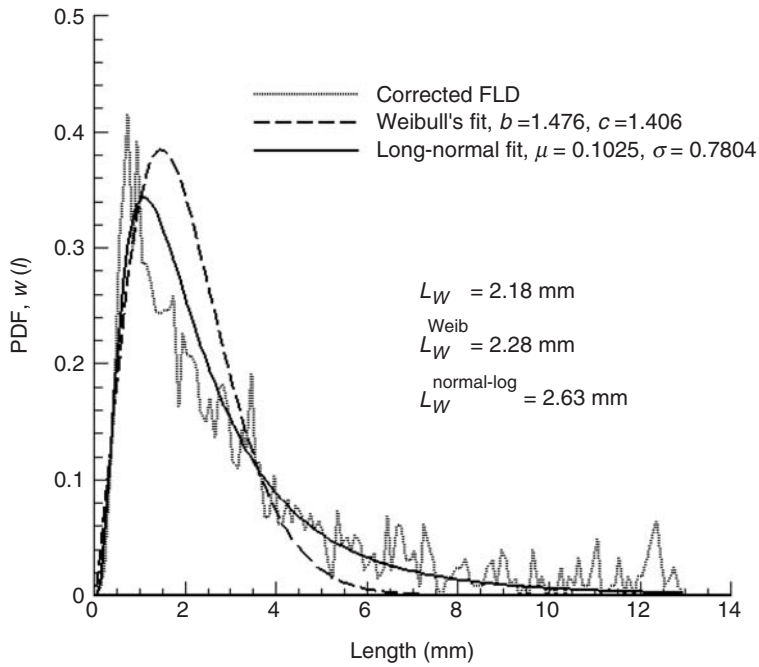

Figure 5. *FLDs in terms of probability density function for weight of fibers vs. fiber length for the slow-fill center-gated disk (Region B).*

Downloaded from jcm.sagepub.com at OAK RIDGE NATIONAL LABORATORY on October 5, 2015

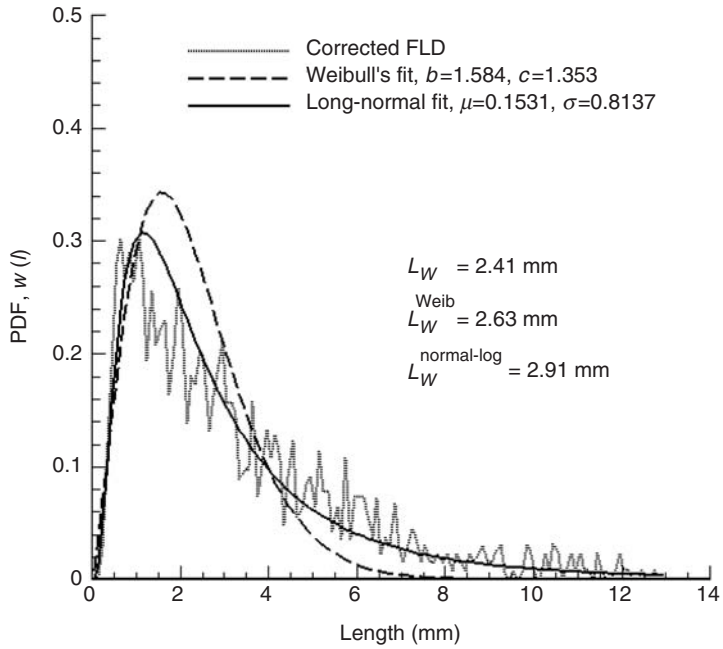

Figure 6. *FLDs in terms of probability density function for weight of fibers vs. fiber length for the slow-fill ISO-plaque (Region B).*

then used to predict fiber orientation in the studied LFT specimens. ORIENT assumes symmetry about the mid-plane in the thickness direction, and this is reflected in the orientation predictions: the predicted values of A_{11}, A_{22}, and A_{33} are all symmetric about $z = 0$, while A_{31} is anti-symmetric about $z = 0$. The finite difference mesh used in ORIENT consisted of 21 nodes in the thickness direction and 121 nodes in the flow direction. In the simulations [26], the parameter κ in Equation (27) was taken to be 1/30, and parameters b_i $(i = 1, \ldots, 5)$ were chosen as: $b_1 = 7.848 \times 10^{-4}$, $b_2 = 2.357 \times 10^{-2}$, $b_3 = 1.0 \times 10^{-2}$, $b_4 = 1.168 \times 10^{-5}$, and $b_5 = -3.0 \times 10^{-3}$.

The orientation predictions are a good fit to all the experimental orientation data for the LFT glass/PP samples, as shown in Figures 7–10. Compared to the predictions by the RSC model discussed in Ref. [1], the new orientation model captures the through-thickness variations of all components of the second-order orientation tensor much more accurately. Table 5 presents the through-thickness averages of the experimental values of A_{11} and A_{22} for all the studied specimens. It is found that the injection rate has very little effect on the orientation distribution in the center-gated disks.

Prediction of Elastic Properties

The effects of fiber length and orientation on the elastic properties of LFTs were studied in Ref. [1]. An in-house computer code named 'EMTA' was developed that implements the Eshelby–Mori–Tanaka mean field approach and the fiber orientation averaging technique (Equations (1)–(5)) to compute the elastic stiffness of a discontinuous fiber composite. This section applies EMTA to first compute the elastic properties of the

Downloaded from jcm.sagepub.com at OAK RIDGE NATIONAL LABORATORY on October 5, 2015

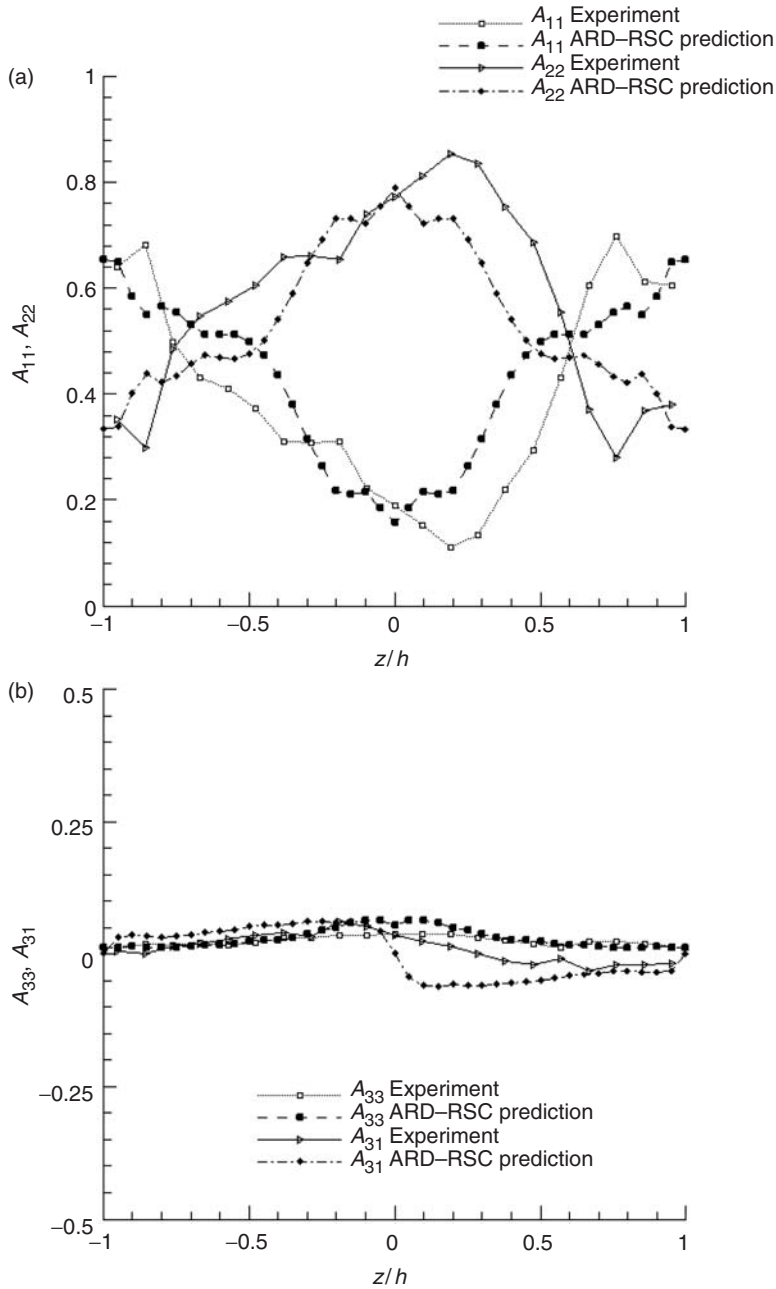

Figure 7. *Predicted and measured second-order orientation components for the fast-fill center-gated disk: (a) A_{11} and A_{22}, (b) A_{33} and A_{31}.*

injection-molded long-glass/PP samples. The elastic moduli and Poisson's ratios of glass fibers and of the PP matrix used in the computation are 73 and 1.5 GPa, and 0.25 and 0.4, respectively [1]. The predictions that used fiber orientation distribution (FOD) results predicted by the ARD model are compared with the solutions based on measured fiber

Downloaded from jcm.sagepub.com at OAK RIDGE NATIONAL LABORATORY on October 5, 2015

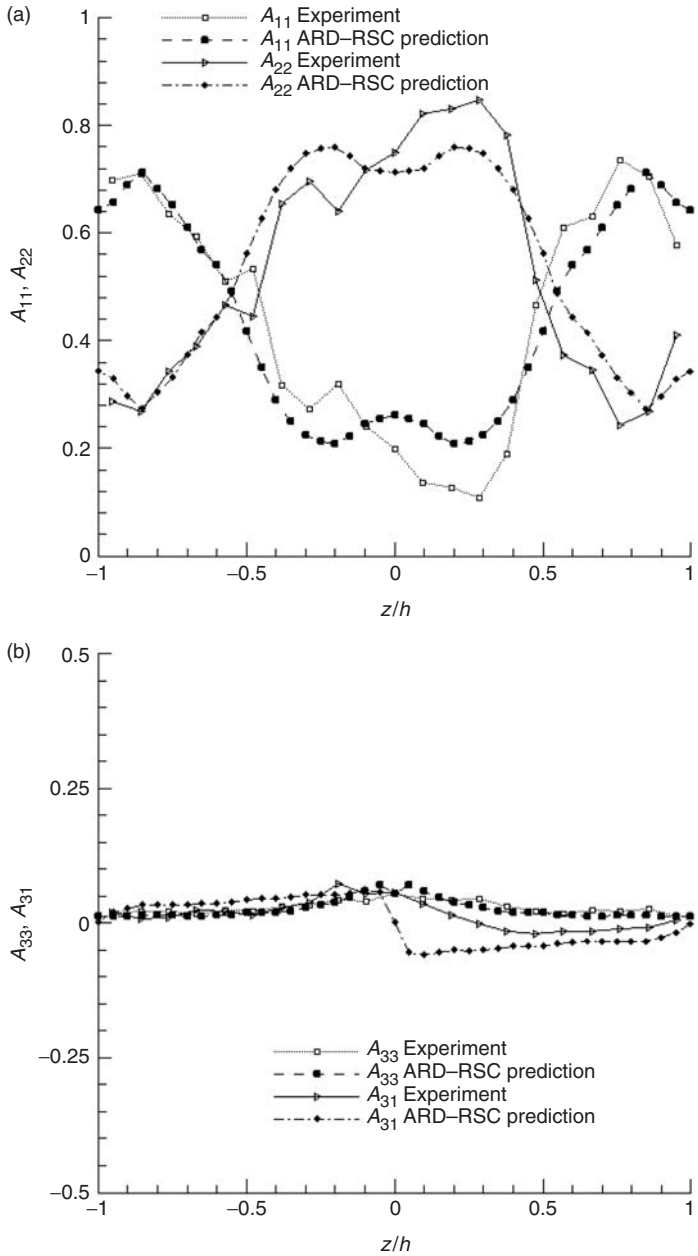

Figure 8. *Predicted and measured second-order orientation components for the fast-fill ISO-plaque: (a) A_{11} and A_{22}, (b) A_{33} and A_{31}.*

orientations and with the experimental results. Tables 1 and 2 give the predicted and experimental moduli for the fast- and slow-fill center-gated disks while Tables 3 and 4 provide the results for fast- and slow-fill ISO-plaques. The average values of the experimental moduli for each direction (flow or cross-flow direction) are also provided in these tables. There are generally good agreements of results for all cases.

Downloaded from jcm.sagepub.com at OAK RIDGE NATIONAL LABORATORY on October 5, 2015

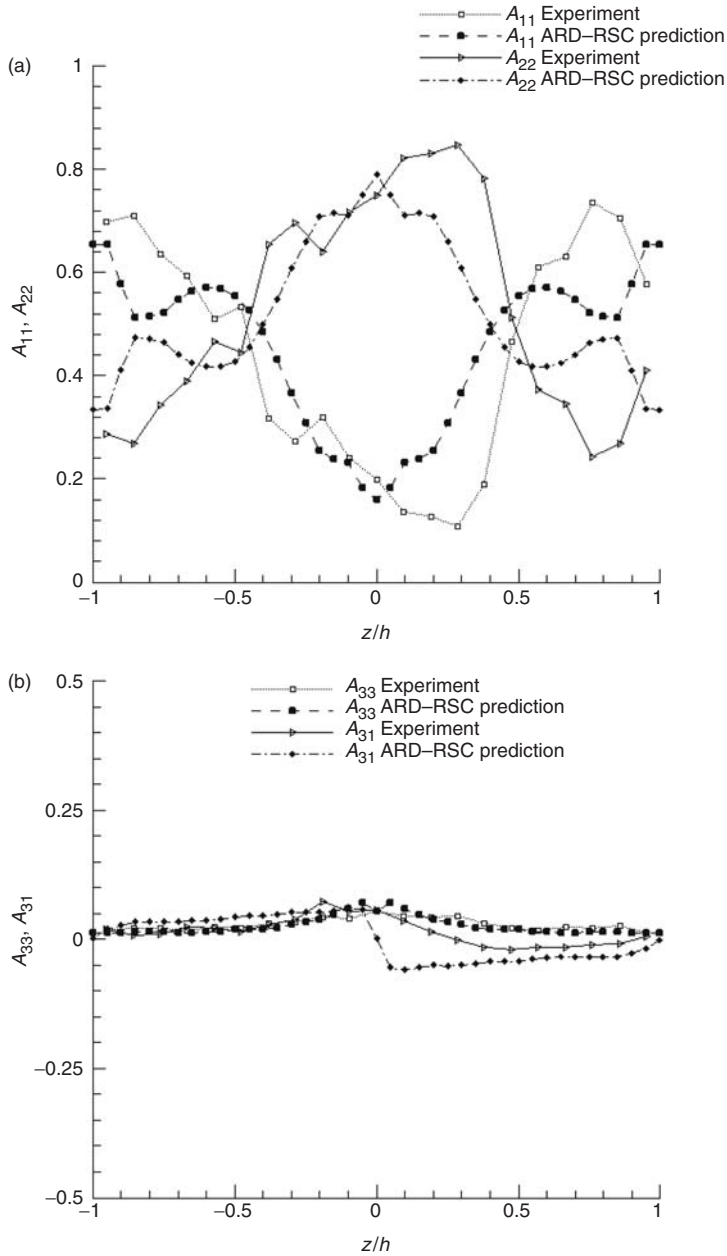

Figure 9. *Predicted and measured second-order orientation components for the slow-fill center-gated disk: (a) A_{11} and A_{22}, (b) A_{33} and A_{31}.*

Prediction of Stress–Strain Responses

The developed elastic–plastic and strength prediction model implemented in ABAQUS was employed to compute the composite stress–strain response using the composite multilayer shell element of this code. The number of layers considered in the analysis was

Downloaded from jcm.sagepub.com at OAK RIDGE NATIONAL LABORATORY on October 5, 2015

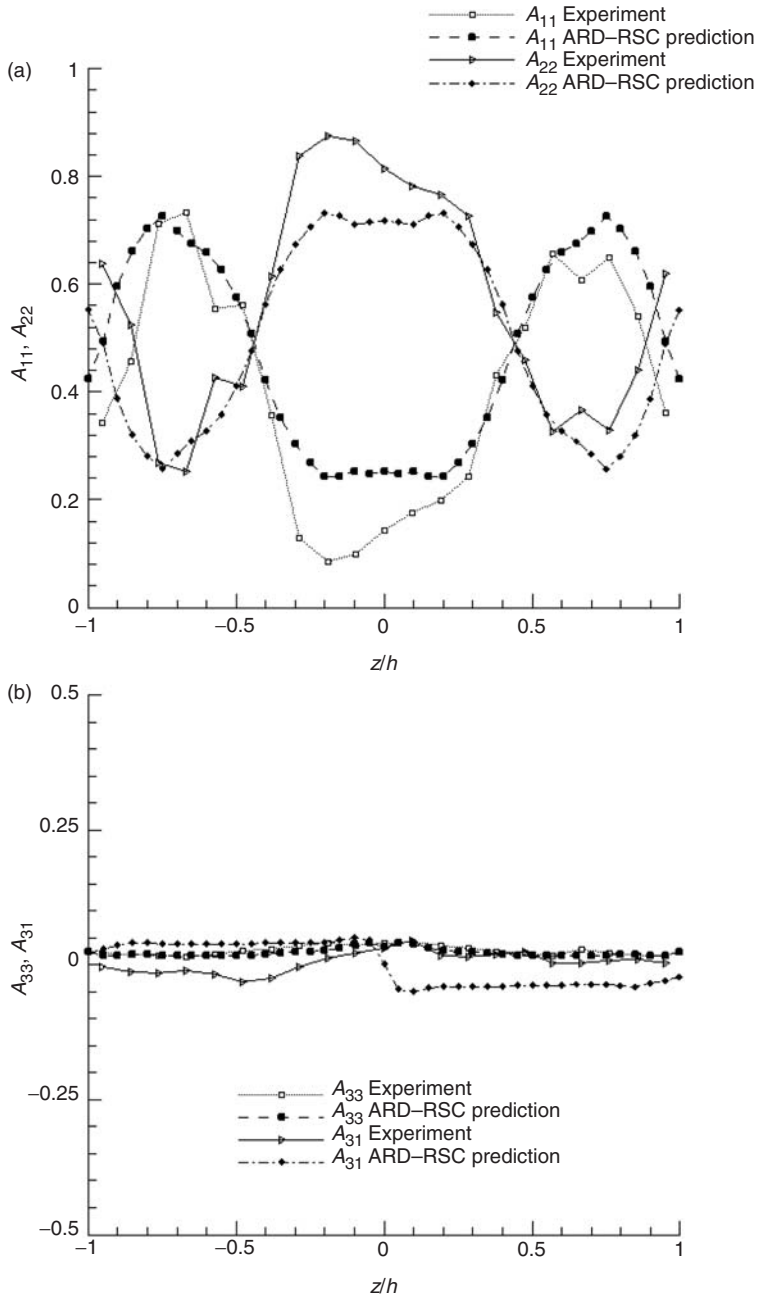

Figure 10. *Predicted and measured second-order orientation components for the slow-fill ISO-plaque: (a) A_{11} and A_{22}, (b) A_{33} and A_{31}.*

based on the number of through-thickness locations at which fiber orientation data were determined. For instance, there were 21 equally spaced through-thickness positions taken for fiber orientation measurement; this then allowed a 21-layer composite shell element to be defined and used in the analysis that accounted for *measured* fiber orientation.

Downloaded from jcm.sagepub.com at OAK RIDGE NATIONAL LABORATORY on October 5, 2015

Table 1. Predicted and experimental overall elastic properties for the fast-fill center-gated disk region B.

	Predictions (experimental FOD and FLD)	Predictions (predicted FOD and experimental FLD)	Experiments
$\overline{E}_{11}$ (MPa)	5540	5833	5199
$\overline{E}_{22}$ (MPa)	7699	6995	7577
$\overline{E}_{33}$ (MPa)	3056	3064	
$\overline{G}_{12}$ (MPa)	2118	2216	
$\overline{G}_{13}$ (MPa)	950	988	
$\overline{G}_{23}$ (MPa)	1012	1017	

Table 2. Predicted and experimental overall elastic properties for the slow-fill center-gated disk region B.

	Predictions (experimental FOD and FLD)	Predictions (predicted FOD and experimental FLD)	Experiments
$\overline{E}_{11}$ (MPa)	5550	6039	5318
$\overline{E}_{22}$ (MPa)	7907	6764	7521
$\overline{E}_{33}$ (MPa)	3068	3068	
$\overline{G}_{12}$ (MPa)	2045	2237	
$\overline{G}_{13}$ (MPa)	940	977	
$\overline{G}_{23}$ (MPa)	1014	993	

Table 3. Predicted and experimental overall elastic properties for the fast-fill ISO-plaque region B.

	Predictions (experimental FOD and FLD)	Predictions (predicted FOD and experimental FLD)	Experiments
$\overline{E}_{11}$ (MPa)	6017	5908	6063
$\overline{E}_{22}$ (MPa)	6935	6951	7211
$\overline{E}_{33}$ (MPa)	3070	3044	
$\overline{G}_{12}$ (MPa)	2046	2110	
$\overline{G}_{13}$ (MPa)	977	966	
$\overline{G}_{23}$ (MPa)	1010	986	

Table 4. Predicted and experimental overall elastic properties for the slow-fill ISO-plaque region B.

	Predictions (experimental FOD and FLD)	Predictions (predicted FOD and experimental FLD)	Experiments
$\overline{E}_{11}$ (MPa)	5784	6408	6166
$\overline{E}_{22}$ (MPa)	7564	6676	7213
$\overline{E}_{33}$ (MPa)	3072	3071	
$\overline{G}_{12}$ (MPa)	2081	2196	
$\overline{G}_{13}$ (MPa)	956	977	
$\overline{G}_{23}$ (MPa)	1018	972	

Downloaded from jcm.sagepub.com at OAK RIDGE NATIONAL LABORATORY on October 5, 2015

Table 5. Averaged experimental through-thickness values of A_{11} and A_{22}.

	Fast-Fill disk	Slow-Fill disk	Fast-Fill plaque	Slow-Fill plaque
Average A_{11}	0.3921	0.3835	0.4433	0.4074
Average A_{22}	0.5830	0.5925	0.5278	0.5661

On the other hand, fiber orientation predictions using 21 nodes through the specimen's half-thickness led to a 41-layer composite shell element that was used in the analysis accounting for *predicted* fiber orientation.

The parameters of the Ramberg–Osgood relation and the strength data for the PP matrix are not known. As the stress–strain response of the PP matrix is different from that of NEAT PP (because of the difference in microstructure), and it is impossible to directly identify the stress–strain response of the PP matrix, we have then indirectly identified the PP matrix's behavior from the experimental stress–strain responses of the longitudinal glass/PP specimens cut from a slow-fill ISO-plaque. Initial guesses for the values of the Ramberg–Osgood coefficients and strength parameters were used in the simulation of the stress–strain response for these specimens up to failure. Necessary parameter adjustments were carried out through simulations until the predicted response agrees with the experimental stress–strain curves. The final values of the parameters for the PP matrix were then identified and used for all the other specimens removed from disks or plaques. The following values for the PP matrix in the studied specimens have been identified: $E_m = 1500\,\text{MPa}$, $\sigma_0 = 8\,\text{MPa}$, $n = 4$, $\overline{\sigma}_m^s = 14\,\text{MPa}$, and $\tau = 7\,\text{MPa}$. The value of the interfacial strength, τ identified is close to the value used by Thomason for a glass/PP system [36].

The strength of E-glass fibers based on [37] is $\sigma_f = 3445$ MPa. The longitudinal strength of the UD composite was then determined using Equations (17) and (18) assuming that $\sigma_m^* = \overline{\sigma}_m^s$. In fact, the exact value of σ_m^* is not known and its choice is still subject of debate. As a first approximation, σ_m^* was taken to be equal to the matrix strength. The strength parameters of the actual LFT composites were obtained by Equation (22) and the fiber orientation data presented in Figures 7–10.

It is first necessary to assess the effect of fiber length representation (Weibull's or Log-normal distribution) on the composite stress–strain response up to failure. To this end, probability density functions for weight of fibers vs. fiber length for the region B of a slow-fill glass/PP ISO-plaque (see Figure 6) were used to predict the stress–strain response of a longitudinal specimen cut from this plaque. Figure 11 shows the comparison of the predicted responses with the experimental results. The predicted curves have a steep and negative slope after the initial failure due to the vanishing element technique used that quickly relaxes the stress and stiffness at the failure location. The stress is then redistributed over the adjacent layers around the failure location, and the neighboring regions will in turn fail. It is clearly seen in Figure 11 that the solution that used the Weibull's distribution has under-predicted the specimen strength while the predictions using the measured FLD and the log-normal distribution are very close to one another and are in better agreement with the experimental results. These findings are not surprising since the Weibull's distribution under-represents the weight contribution of long fibers (>4 mm) that enhance composite's strength. For the validation of the elastic–plastic and strength prediction model, the corrected measured FLDs were used for all the studied specimens.

Figure 12(a) and (b), respectively show the longitudinal (flow direction) and in-plane transverse (cross-flow direction) stress–strain responses for the fast-fill center-gated disk.

Downloaded from jcm.sagepub.com at OAK RIDGE NATIONAL LABORATORY on October 5, 2015

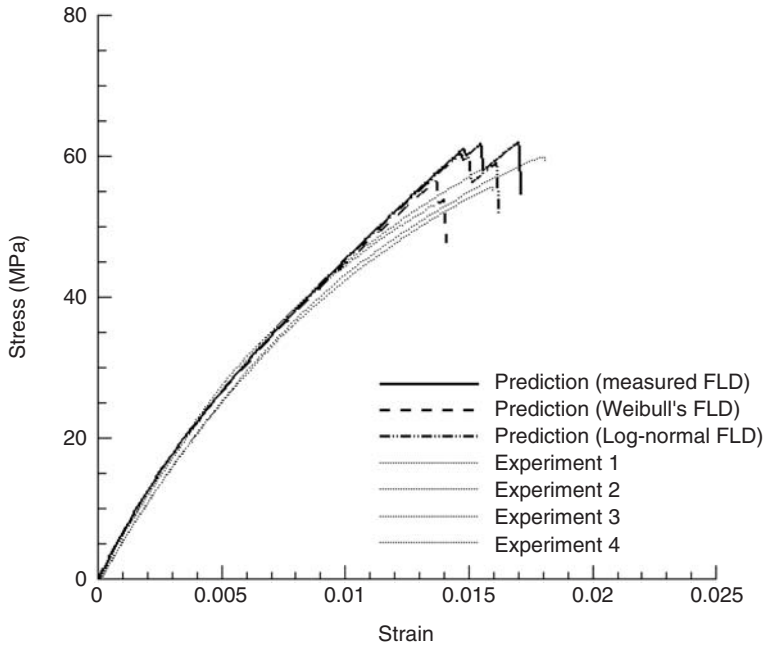

Figure 11. *The effect of FLD representation on the stress–strain response predicted for a longitudinal specimen removed from a slow-fill glass/PP ISO-plaque.*

These figures show that the responses predicted using measured fiber orientation or predicted fiber orientation by the ARD–RSC model are pretty close to one another. Furthermore, the correlation of either prediction with the experimental results is better for the in-plane transverse behavior. This suggests that more progressive damage occurs in the longitudinal specimens, contributing to the more pronounced nonlinearity displayed by those specimens. The other reason is due to the fiber orientation effect. The simulation used the FOD data determined for region B whereas the specimens although contain region B, they also cover adjacent regions whose FODs can be noticeably different from the FOD at region B.

Figure 13(a) and (b) present the results for the fast-fill ISO plaque. The same observations as in the previous case apply to this case. However, there is better agreement between the predicted responses with the experimental curves in the longitudinal direction of the ISO plaque, compared to the flow direction for the fast-fill center-gated disk. Again, the more pronounced nonlinearity in the flow direction suggests more contribution of matrix nonlinear behavior and that more damage is occurring when the specimen is loaded in this direction. In fact, the fiber orientation distributions in Figures 7 and 8 show that, on average, the cross-flow A_{22} component is higher than the A_{11} component in both the ISO plaque and the disk. Therefore, the fibers are more aligned in the cross-flow direction than in the flow direction, leading to a greater portion of the stress carried by the matrix under flow-direction loading. As a result, greater amounts of plastic deformation and of progressive damage by matrix cracking and fiber/matrix debonding occur in the flow-direction specimen, producing a more pronounced nonlinearity in the longitudinal stress–strain responses.

The results for the slow-fill center-gated disk and ISO-plaque are given in Figure 14(a) and (b) and Figure 15(a) and (b), respectively. Similar conclusions to the fast-fill cases can be

Downloaded from jcm.sagepub.com at OAK RIDGE NATIONAL LABORATORY on October 5, 2015

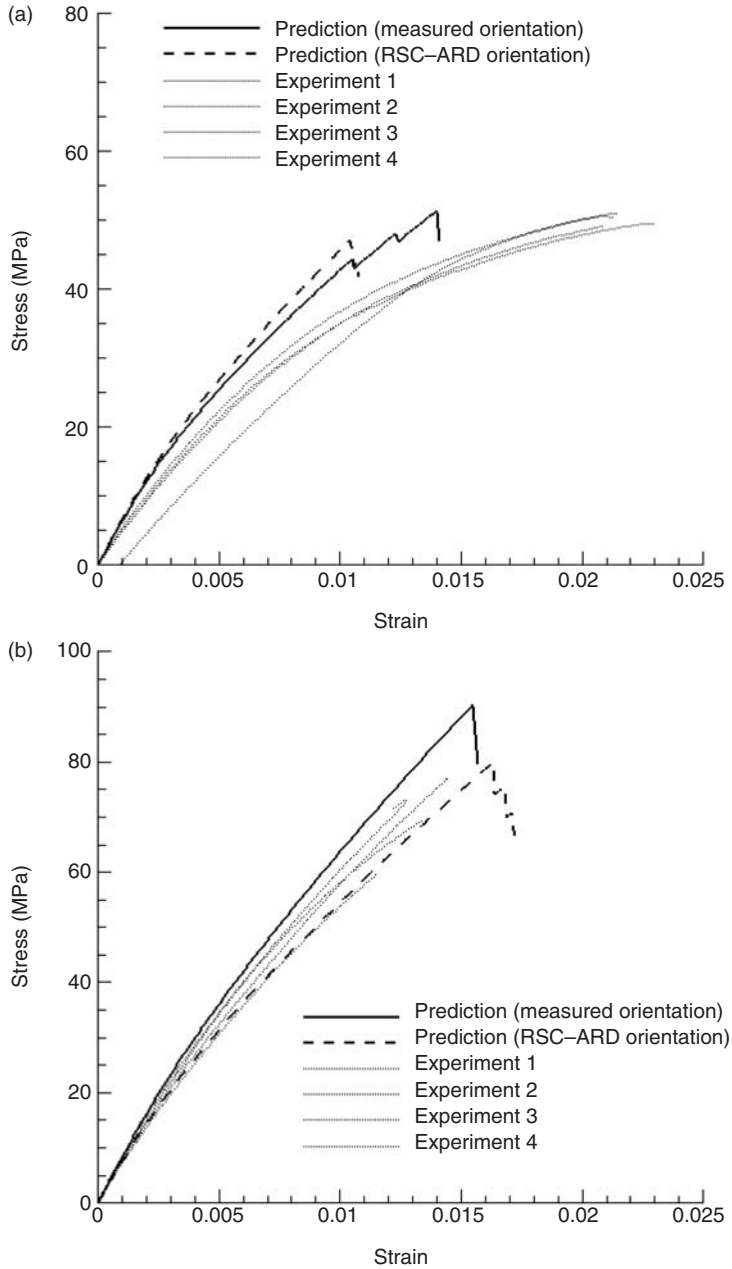

Figure 12. *Predicted and experimental (a) longitudinal and (b) in-plane transverse stress/strain responses for the fast-fill center-gated disk.*

drawn for the slow-fill cases. The current model reasonably well captures the stress–strain responses in both flow and cross-flow directions; however, it will be necessary to model progressive damage, in addition to plasticity, in order to better capture the more pronounced nonlinearity observed in the flow-direction stress–strain responses at the approach of final failure.

Downloaded from jcm.sagepub.com at OAK RIDGE NATIONAL LABORATORY on October 5, 2015

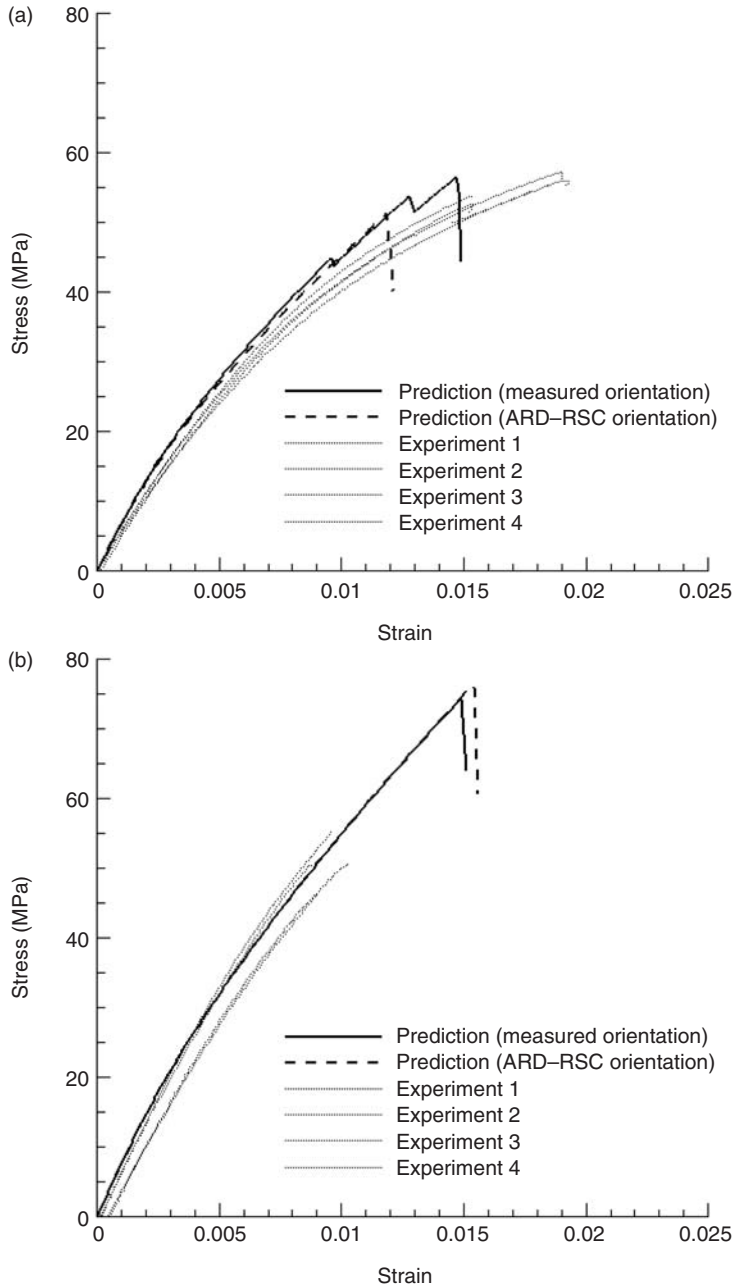

Figure 13. *Predicted and experimental (a) longitudinal and (b) in-plane transverse stress/strain responses for the fast-fill ISO-plaque.*

The strengths predicted for all the slow- and fast-fill cases are given in Tables 6 and 7. The averaged experimental strength values are also provided in these tables. To have a good insight of these results, it is necessary to examine the FLDs provided in Figures 3–6, and Table 1 which gives the thickness-average values of the orientation components

Downloaded from jcm.sagepub.com at OAK RIDGE NATIONAL LABORATORY on October 5, 2015

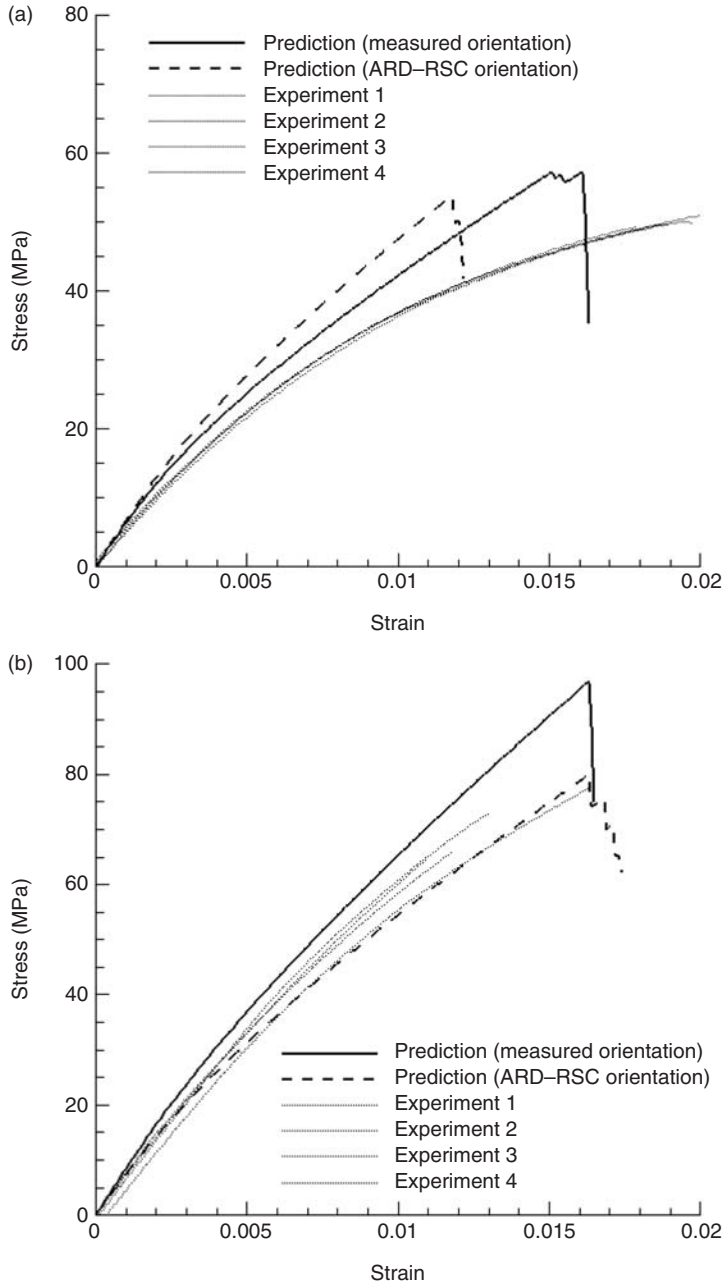

Figure 14. *Predicted and experimental (a) longitudinal and (b) in-plane transverse stress/strain responses for the slow-fill center-gated disk.*

A_{11} and A_{22} for all the studied samples. Also, it is necessary to examine the actual fiber orientation distribution in the in-plane transverse specimens removed from ISO-plaques.

First, the experimental slow-fill and fast-fill disk results (Figures 12 and 14) are nearly identical within the experimental scatter, this is because these samples have practically the

Downloaded from jcm.sagepub.com at OAK RIDGE NATIONAL LABORATORY on October 5, 2015

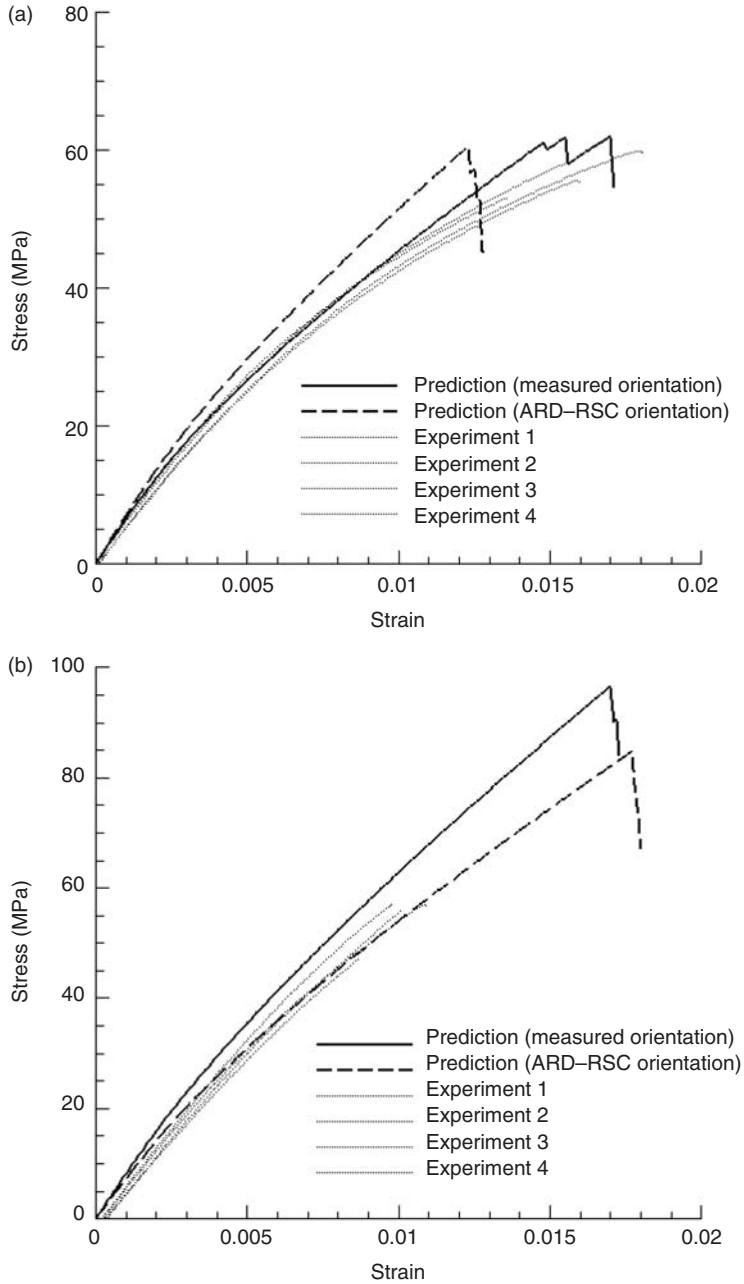

Figure 15. *Predicted and experimental (a) longitudinal and (b) in-plane transverse stress/strain responses for the slow-fill ISO-plaque.*

same fiber length distribution and thickness-average values of A_{11} and A_{22}. Second, the average A_{11} and A_{22} in the fast-fill and slow-fill ISO-plaques are also nearly identical within the experimental scatter, however, the slow-fill injection rate has conserved longer fibers, and this results in the stiffer and stronger slow-fill ISO-plaque (Figure 15 compared to Figure 13).

Downloaded from jcm.sagepub.com at OAK RIDGE NATIONAL LABORATORY on October 5, 2015

Table 6. Predicted and experimental flow direction strengths for the fast-fill glass/PP samples.

Specimen (fast-fill)	Flow direction strength (measured fiber orientation) (MPa)	Flow direction strength (predicted fiber orientation) (MPa)	Experiment (MPa)
Center-gated disk	51.3	47.1	50.1
ISO-plaque	56.5	51.3	54.8
Specimen (fast-fill)	**Cross-flow direction strength (measured fiber orientation)**	**Cross-flow direction strength (predicted fiber orientation)**	**Experiment**
Center-gated disk	90.4	75.5	69.8
ISO-plaque	74.4	76.5	50.8

Table 7. Predicted and experimental flow direction strengths for the slow-fill glass/PP samples.

Specimen (Slow-fill)	Flow direction strength (measured fiber orientation) (MPa)	Flow direction strength (predicted fiber orientation) (MPa)	Experiment (MPa)
Center-gated disk	57.3	53.8	50.1
ISO-plaque	62	60.6	56.7
Specimen (Slow-fill)	**Cross-flow direction strength (measured fiber orientation)**	**Cross-Flow direction strength (predicted fiber orientation)**	**Experiment**
Center-gated disk	96.8	79.9	70.4
ISO-plaque	96.5	84.7	54.3

Finally, the strength predictions for longitudinal specimens agree reasonably well with the experimental results while the strengths predicted for in-plane transverse specimens removed from plaques are significantly higher than the experimental values. The main cause of this deviation is due to a fiber orientation effect. The actual in-plane transverse specimens possess fiber orientation distributions that are more in alignment with the flow direction around the specimens' ends (near the grips) due to an edge effect occurring during injection molding. When these specimens were subjected to tensile loading, the matrix material was more exposed to loading resulting in early failure initiation of the specimens in these locations.

CONCLUSIONS

An elastic–plastic model for long-fiber thermoplastic composites has been developed, using an incremental Eshelby–Mori–Tanaka approach to compute the homogenized nonlinear stress–strain response. The model considers the elastic–plastic behavior of the thermoplastic matrix and elastic long fibers, whose length distribution is represented by a Weibull's or a log-normal probability density function for weight of fibers vs. fiber length. In addition, the model accounts for the fiber orientation distribution resulting from the molding process. The elastic–plastic matrix obeys the Ramberg–Osgood relation and the *J*-2 deformation theory of plasticity. The Van Hattum–Bernado failure criterion has been

Downloaded from jcm.sagepub.com at OAK RIDGE NATIONAL LABORATORY on October 5, 2015

associated with the elastic–plastic model to predict strength of LFTs. The entire model has been implemented in the ABAQUS finite element code by means of user subroutines, and a multi-layer shell element has been used in the analysis of LFT glass/PP specimens subjected to tensile loading. Fiber orientation and fiber length distributions were measured for all the studied specimens. In addition, fiber orientations were also predicted using the newly developed ARD–RSC model. The following important conclusions are drawn from our study:

- Good prediction of fiber orientation by the ARD–RSC model allows more accurate predictions of the stress–strain response of LFTs. The predicted stress–strain responses using predicted fiber orientations are close to the predicted curves based on measured orientations.
- Weibull's probability density function for weight of fibers vs. fiber length can sufficiently represent fiber length distribution for use only in the computation of elastic properties. However, it fairly represents the FLD for use in strength prediction as it under-represents the contribution of long fibers (>4 mm) that enhance the overall strength of the composite. The log-normal distribution is more appropriate to represent FLDs for strength prediction.
- The nonlinear stress–strain responses of the studied glass/PP specimens are mainly due to the nonlinear stress–strain behavior of the matrix PP.
- The Van Hattum–Bernado model can reasonably well predict the strengths of LFTs. Associating this model with the present elastic–plastic model for LFTs is a first step to predict the strengths of these materials. Nevertheless, as the failure criterion ignores any damage processes, it cannot predict strength to a high level of accuracy.
- Finally, it will be necessary to model progressive damage to better capture the nonlinear stress–strain response up to failure in order to predict composite's strength more accurately.

ACKNOWLEDGMENTS

This study has been funded by the U.S. Department of Energy's Office of FreedomCAR and Vehicle Technologies. The support by Dr. Joseph Carpenter Jr., Technology Area Development Manager, is gratefully acknowledged. We would like to thank Moldflow, Inc. for the rheological and physical data measurement for the glass/polypropylene material studied in this article.

REFERENCES

1. Nguyen, B.N., Bapanapalli, S.K., Holbery, J.D., Smith, M.T., Kunc, V., Frame, B.J., Phelps, J.H. and Tucker III, C.L. (2008). Fiber Length and Orientation Distributions in Long-Fiber Injection-Molded Thermoplastics – Part I: Modeling of Microstructure and Elastic Properties, *Journal of Composite Materials*, **42**: 1003–1029.
2. Tucker III, C.L., Wang, J. and O'Gara J.F. (2007). Method and Article of Manufacture for Determining a Rate of Change of Orientation of a Plurality of Fibers Disposed in a Fluid. U.S. Patent No. 7,266,469. See also Wang, J., O'Gara, J. F., and Tucker, III C.L. (2007). An Objective Model for Slow Orientation Kinetics in Concentrated Fiber Suspensions: Theory and Rheological Evidence. *Journal of Rheology* (submitted).

Downloaded from jcm.sagepub.com at OAK RIDGE NATIONAL LABORATORY on October 5, 2015

3. Nguyen, B.N. and Khaleel, M.A. (2003). Prediction of Damage in a Randomly Oriented Short-Fiber Composite Plate Containing a Central Hole, In: Bathe, K.J. (ed.), *Computational Fluid and Solid Mechanics*, pp. 519–522, Elsevier Ltd, Oxford, UK.
4. Nguyen, B.N. and Khaleel, M.A. (2004). A Mechanistic Approach to Damage in Short-Fiber Composites Based on Micromechanical and Continuum Damage Mechanics Descriptions, *Composite Science and Technology*, **64**: 607–617.
5. Nguyen, B.N., Tucker, B.J. and Khaleel, M.A. (2005). A Mechanistic Approach to Matrix Cracking Coupled with Fiber-Matrix Debonding in Short-Fiber Composites, *Journal of Engineering Materials and Technology*, **127**: 337–350.
6. Eshelby, J.D. (1957). The Determination of the Elastic field of an Ellipsoidal Inclusion and Related Problems, In: *Proceedings of the Royal Society London*, **A241**: 376–396.
7. Mori, T. and Tanaka, K. (1973). Average Stress in Matrix and Average Elastic Energy of Materials with Misfitting Inclusions, *Acta Metallurgica*, **21**: 571–574.
8. Laws, N., Dvorak, G.J. and Hejazi (1983). Stiffness Changes in Unidirectional Composites Caused by Crack Systems, *Mechanics of Materials*, **2**: 123–137.
9. Qu, J. (1993). The Effect of Slightly Weakened Interfaces on the Overall Elastic Properties of Composite Materials, *Mechanics of Materials*, **14**: 269–281.
10. Galeski, A. (2003). Strength and Toughness of Crystalline Polymer Systems, *Progress in Polymer Science*, **28**: 1643–1699.
11. Arsenault, R.J. and Taya, M. (1987). Thermal Residual Stress in Metal Matrix Composite, *Acta Metallugica*, **35**(3): 651–659.
12. Tandon, G.P. and Weng, G.J. (1988). A Theory of Particle-Reinforced Plasticity, *Journal of Applied Mechanics*, **55**: 126–135.
13. Dunn, M.L. and Ledbetter, H. (1997). Elastic–Plastic Behavior of Textured Short-Fiber Composites, *Acta Materialia*, **45**(8): 3327–3340.
14. Qui, Y.P. and Weng, G.J. (1995). An Energy Approach to the Plasticity of a Two-Phase Composite Containing Aligned Inclusions, *Journal of Applied Mechanics*, **62**: 1039–1046.
15. Pettermann, H.E., Plankensteiner, A.F., Böhm, H.J. and Rammerstorfer, F.G. (1998). A Thermo-Elasto-Plastic Constitutive Law for Inhomogeneous Materials Based on An Incremental Mori–Tanaka Approach, *Computers and Structures*, **71**: 197–214.
16. Gavazzi, A.C. and Lagoudas, D.C. (1990). On the Numerical Evaluation of Eshelby's Tensor and Its Application to Elastoplastic Fibrous Composites, *Computational Mechanics*, **7**: 13–19.
17. Doghri, I. and Ouaar, A. (2003). Homogenization of Two-Phase Elasto-Plastic Composite Materials and Structures – Study of Tangent Operators, Cyclic Plasticity and Numerical Algorithm, *International Journal of Solids and Structures*, **40**: 1681–1712.
18. Doghri, I. and Tinel, L. (2005). Micromechanical Modeling and Computation of Elasto-Plastic Materials Reinforced with Distributed-Orientation Fibers, *International Journal of Plasticity*, **21**: 1919–1940.
19. Doghri, I. and Tinel, L. (2006). Micromechanics of Inelastic Composites with Misaligned Inclusions: Numerical Treatment of Orientation, *Computer Methods in Applied Mechanics and Engineering*, **195**: 1387–1406.
20. Pierard, O., Gonzalez, C., Segurado, J., Llorca, J. and Doghri, I. (2007). Micromechanics of Elasto-Plastic Materials Reinforced with Ellipsoidal Inclusions, *International Journal of Solids and Structures*, **44**: 6945–6962.
21. Ramberg, W. and Osgood, W.R. (1943). Description of Stress–Strain Curves by Three Parameters, Technical Note No. 902, National Advisory Committee for Aeronautics, Washington DC.
22. Advani, S. and Tucker III, C.L. (1987). The Use of Tensors to Describe and Predict Fiber Orientation in Short-Fiber Composites, *Journal of Rheology*, **31**: 751–784.
23. Camacho, C., Tucker III, C.L., Yalvac, S. and McGee, R.L. (1990). Stiffness and Thermal Expansion Predictions for Hybrid Short-Fiber Composites, *Polymer Composites*, **11**: 229–239.
24. Van Hattum, F.W.J. and Bernado, C.A. (1999). A Model to Predict the Strength of Short Fiber Composite, *Polymer Composites*, **20**(4): 524–533.

Downloaded from jcm.sagepub.com at OAK RIDGE NATIONAL LABORATORY on October 5, 2015

25. Tsai, S.W. and Wu, E.M. (1971). A General Theory of Strength for Anisotropic Materials, *Journal of Composite Materials*, **5**: 58–80.
26. Phelps, J.H. and Tucker III, C.L. (2008). An Anisotropic Rotary Diffusion Model for Fiber Orientation in Short- and Long-Fiber Thermoplastics, *Journal of the Non-Newtonian Fluid Mechanics*, submitted.
27. Cintra, Jr., J.S. and Tucker III, C.L. (1995). Orthotropic Closure Approximations for Flow-Induced Fiber orientation, *Journal of Rheology*, **39**: 1095–1122.
28. Wetzel, E.D. (1999). Modeling Flow-Induced Microstructure in Inhomogeneous Liquid-Liquid Mixtures, PhD thesis, University of Illinois at Urbana-Champaign, Urbana, IL.
29. Kelly, A. and Tyson, W.R. (1965). Tensile Properties of Fibre-Reinforced Metals: Copper/Tungsten and Copper/Molybdenum, *Journal of the Mechanics and Physics of Solids*, **13**: 329–350.
30. Folgar, F. and Tucker III, C.L. (1984). Orientation Behavior of Fibers in Concentrated Suspensions, *Journal of Reinforced Plastic Composites*, **3**: 98–119.
31. Fan, X., Phan-Thien, N. and Zheng, R. (1998). A Direct Simulation of Fibre Suspension, *Journal of Non-Newtonian Fluid Mechanics*, **74**: 113–135.
32. Phan-Thien, N., Fan, X.-J., Tanner, R.I. and Zheng R. (2002). Folgar-Tucker Constant for a Fibre Suspension in a Newtonian Fluid, *Journal of Non-Newtonian Fluid Mechanics*, **103**: 251–260.
33. Kunc, V., Frame, B.J., Nguyen, B.N., Tucker III, C.L. and Velez-Garcia, G. (2007). Fiber Length Distribution Measurement for Long Glass and Carbon Fiber Reinforced Injection Molded Thermoplastics. In: *Proceedings of the 7th Annual SPE Automotive Composites Conference and Exposition*, Society of Plastic Engineers, Troy, Michigan.
34. Hine, P.J., Davidson, N., Duckett, R.A., Clarke, A.R. and Ward, I.M. (1996). Hydrostatically Extruded Glass-Fiber-Reinforced Polyoxymethylene. I: The Development of Fiber and Matrix Orientation, *Polymer Composites*, **17**: 720–729.
35. Bay, R.S. and Tucker III, C.L. (1992). Fiber Orientation in Simple Injection Moldings. Part I: Theory and Numerical Methods. *Polymer Composites*, **13**: 317–331.
36. Thomason, J.L. (2002). Interfacial Strength in Thermoplastic Composites – At Last an Industry Friendly Measurement Method? *Composites – Part A: Applied Science and Manufacturing*, **33**: 1283–1288.
37. Miller, D.M. (1987). Glass Fibers, In: Composites, Vol. 1: Engineered Materials Handbook, ASM International, Ohio, pp. 45–48.

Downloaded from jcm.sagepub.com at OAK RIDGE NATIONAL LABORATORY on October 5, 2015